energies

MDPI

Article

Zero Current Switching Switched-Capacitors Balancing Circuit for Energy Storage Cell Equalization and Its Associated Hybrid Circuit with Classical Buck-Boost

Xiaolin Wang, Ka Wai Eric Cheng * and Yat Chi Fong

Power Electronics Research Center, Department of Electrical Engineering, The Hong Kong Polytechnic University, Hong Kong 999077, China

* Correspondence: eeecheng@polyu.edu.hk

Received: 21 April 2019; Accepted: 28 June 2019; Published: 16 July 2019

Abstract: To overcome the problem of switching loss during the balancing process, a novel cell balancing circuit is proposed with the integration of a zero current switching technique. Moreover, the balancing circuit proposed can change between a classical buck-boost pattern and a resonant switched-capacitor pattern with flexible control to cater to the balancing requirements under different driving scenarios. The results of the simulation of field experiments demonstrate successful balancing, various balancing speed, and low energy loss. The proposed balancing circuit proves to be effective for a wide range of application and is the first attempt to integrate a dual balancing function in a single balancing circuit for cells.

Keywords: cell equalization; zero current switching; hybrid circuit

1. Introduction

The pursuit of better battery performance has become the top challenge for electric vehicle (EV) design, as it primarily determines the driving mileage and manufacturing cost [1–4]. With the fast development of a supercapacitor (SC), the battery and SC strings composed of a large number of series and parallel-connected cells are usually used to formulate a hybrid energy package for better power performance [5–8]. Moreover, increasing numbers of researchers are collecting retired batteries for second-life application, hoping to cut costs while maintaining a qualified driving performance. Due to non-uniform individual cell properties, a certain imbalance may be easily generated among voltages of different cells during charging and discharging processes. As the effect of imbalance is accumulative and leads to battery deterioration, voltage balancing is necessary to guarantee the safe operation of the hybrid energy package [9–11].

Researchers have done many state-of-the-art works on promoting the balancing efficiency and balancing speed and decreasing loss. The passive balancing method is the most commonly adopted technique. Resistors in parallel with the cell strings are switched on when the cells get close to the peak withstanding voltage or when they have a higher state-of-charge (SoC) than other cells. This method generates additional heating loss because the energy dissipates into resistors during balancing process [12]. For energy-saving purposes, an active balancing method is put forward so that the charging and discharging current of each cell can be controlled to keep the same SoC among all cell units for the higher energy to be transferred into the cells with lower energy using a power converter circuit, instead of wasting it as heat loss. This method has proven to be more efficient, hence, many advanced voltage equalizers have been designed based on the active method using converters [13,14], switched-capacitors [15–18], transformers [7] or switched inductors [19,20].

However, those methods are not flexible enough for changing scenarios. Furthermore, as a hard switching operation is adopted in a large number of cell balancing circuits [21–23], electromagnetic interference (EMI) and high switching energy loss will appear. On the other hand, the service life of energy sources will also be affected by a current spike in hard switching circuits. In this paper, a novel balancing circuit is proposed to realize zero-current switching (ZCS) similar to quasi-resonant [24,25] during the switched-capacitor mode and has been proven to further reduce energy loss [24–29].

Different states of EVs, such as the drive state, brake state, and park state, may have different requirements on the output power, balancing speed, and balancing loss. Many existing papers [22,23] do not take the real driving state into account and make a fixed cell balancing strategy, which decreases the overall balancing efficiency [30–33]. They are based on switched-capacitor techniques [34,35]. Some papers have realized the difference in energy management at different driving states and proposed specific energy controllers respectively. The energy saving controller for electric mining trucks is introduced in Reference [36], as it runs in high-frequency start-up processes. A predictive energy controller based on preceding vehicle movement management is designed in Reference [37] for lined up EVs on the road. A real-time energy controller for EVs in a charge-depletion mode is discussed in References [38–40] for adaptive energy consumption minimization.

In this paper, a novel and multi-functional balancing circuit is proposed with a ZCS technique to improve energy saving during the balancing process. The multi-functional circuit can easily change between a buck-boost pattern and switched-capacitor pattern with flexible switching frequency and duty ratios, i.e., the circuit can adapt to changing driving states. Figure 1 demonstrates six different operating modes with different cell balancing requirements for the corresponding driving states. Moreover, voltage sensors can be installed at each cell in order to collect the voltage signals for an intelligent control box. In the real-time feedback control, switching frequency and duty ratios are adjusted to accelerate voltage balancing process and decrease loss. This paper is the first attempt to use the ZCS technique in the integrated balancing circuit for rapid mode switching, accurate voltage tracking, and loss reduction. The circuit configuration, operation principle, and equations are presented in Sections 2 and 3. The results of the simulation and field experiment are presented in Sections 4 and 5. Section 6 concludes this paper.

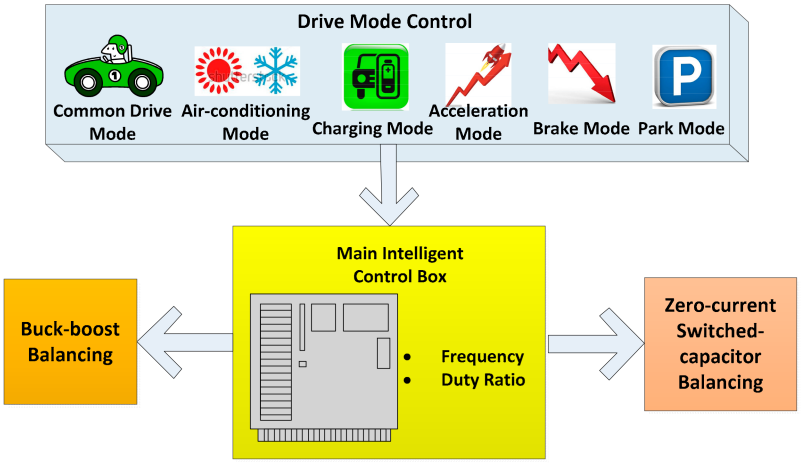

Figure 1. Different operating modes and requirements.

2. Proposed Cell Balancing Circuits

2.1. Circuit Configuration

In this section, a series multi-functional balancing circuit is presented for analysis. Different states of EVs, such as the drive state, brake state, and park state, may have different requirements on the output power, balancing speed, and balancing loss. Figure 1 demonstrates six different operating

modes with different cell balancing requirements for the corresponding driving states. For example, EVs in acceleration desire a high balancing speed and low loss while the park state does not have requirements on the balancing speed. The circuitry of Figure 2 shows the SC cells (SC_1, SC_2, ... , SC_n) in series connection. In the n-cells voltage balancing system, there are $n - 1$ switched-capacitors and $4n - 4$ switches which are dominated by the main intelligent control box to operate the circuit in different modes. All the switches are named in two groups S_a and S_b, the switches in each group are divided as S_{a2m-1}, S_{a2m}, S_{a2m+1} and S_{a2m+2}, where m varies from 1 to $n - 1$; In S_{b2m-1}, S_{b2m}, S_{b2m+1} and S_{b2m+2}, m varies from 1 to $n - 1$. This multi-functional balancing circuit has two operation states, buck-boost balancing and switched-capacitor balancing, under different control of inductors (L_1, L_2, ... , L_{n-1}) and switched-capacitors (C_1, C_2, ... , C_{n-1}). And the charge is transferred from a higher voltage SC to lower ones automatically. The proposed circuit changes its topology and parameters to cater to the operation requirements of different operation modes, such as the common drive mode, drive with air-conditioning mode, acceleration mode, brake mode, and park mode for EVs.

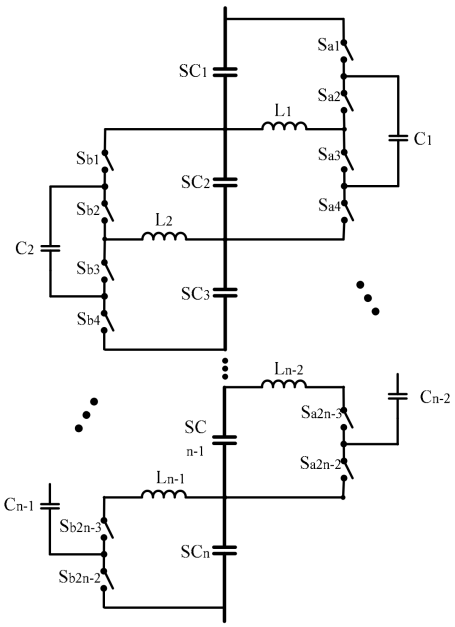

Figure 2. Proposed balancing circuit.

2.2. Balancing Circuit Operation Analysis

In an ideal case, the switching frequency f_s should be equal to the resonant frequency f_r.

$$f_s = f_r = \frac{1}{2\pi}\sqrt{\frac{1}{LC} - \theta^2} \tag{1}$$

where $\theta = \frac{R}{2L}$; R is the equivalent resistance, L is the inductance of the inductor and C is the capacitance of the switched-capacitor.

However, it is arduous to precisely match the RLC parameters of different balancing branches in real implementation. To avoid a reverse current of the resonant inductor, the switching frequency in the proposed switched-capacitor circuit should be slightly higher than the resonant frequency with regards to the tolerances of the RLC parameters.

There are two clock phase φ_a and φ_b in one switching period T, as shown in Figure 3. During the φ_a, the switches S_{a2m-1}, S_{b2m-1} and S_{a2m+1}, S_{b2m+1} are turned on, the circuit forms the switched-capacitors resonant tanks series connecting with switched-capacitors as shown in Figure 4a,b. Meanwhile, Figure 4c,d are in a buck-boost mode state during the φ_b, when S_{a2m-1}, S_{b2m-1} and S_{a2m}, S_{b2m} are turned on, there is only an inductor connect with SC. These two functioning modes operate alternatively with

a high frequency control signal. They are divided into ZCS mode state I, ZCS mode state II, buck-boost mode state I and buck-boost mode state II which will be discussed in Section 2.3.

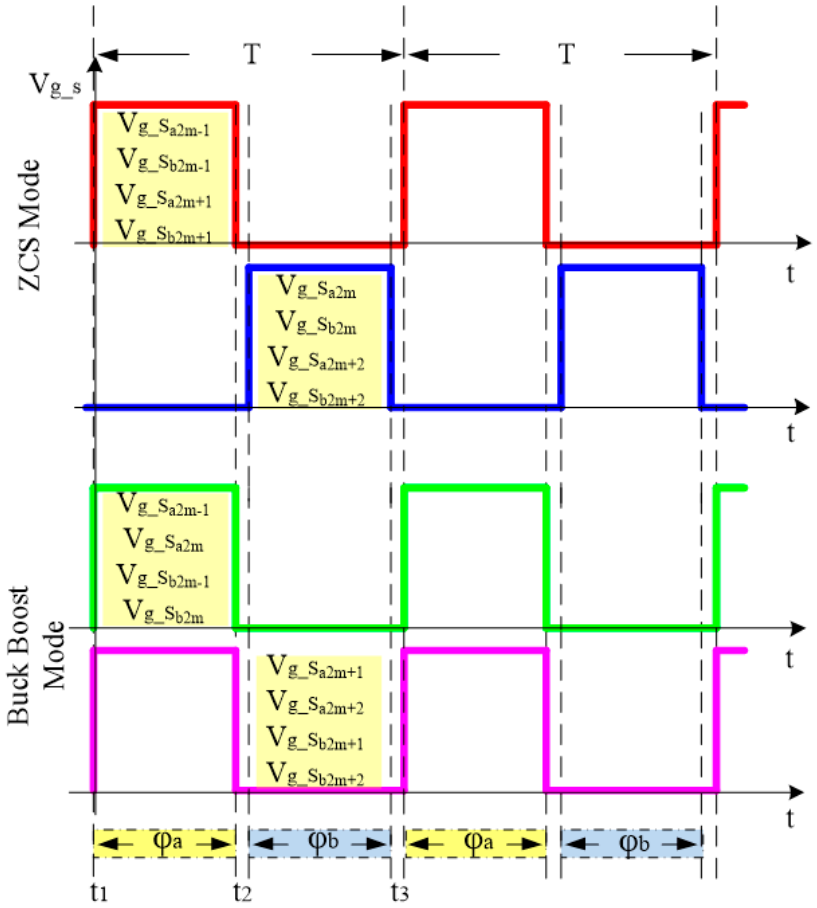

Figure 3. Control signal of the switches.

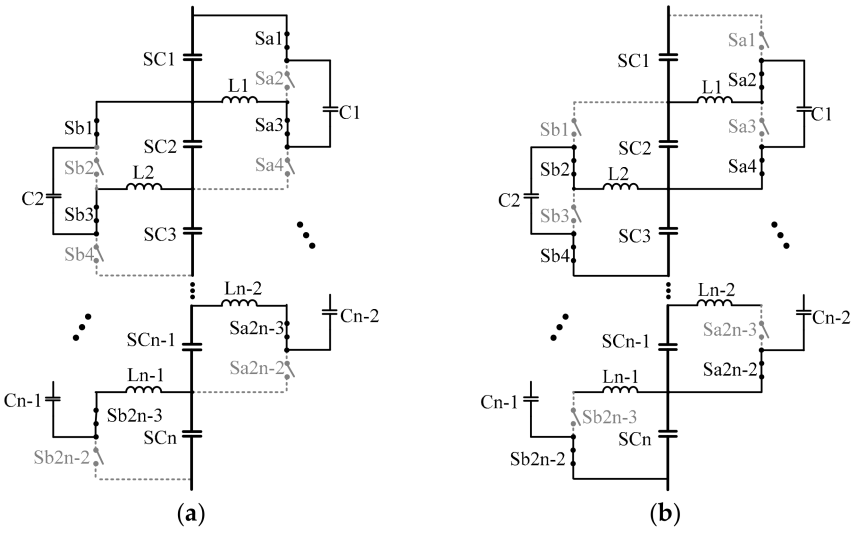

Figure 4. *Cont.*

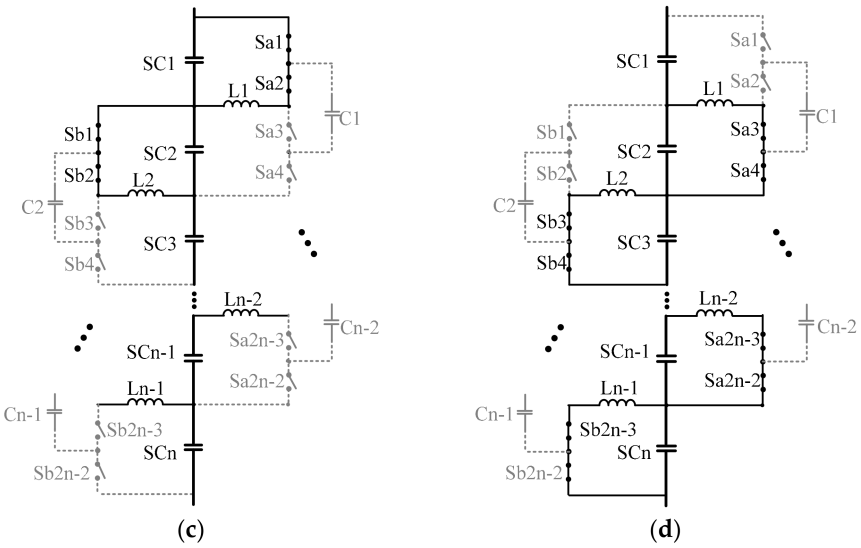

Figure 4. Working principle of the proposed balancing system. (**a**) ZCS mode state I; (**b**) ZCS mode state II; (**c**) buck-boost mode state I; (**d**) buck-boost mode state II.

2.3. Analysis of ZCS Operation

When the switches S_{a2m-1}, S_{b2m-1} and S_{a2m+1}, and S_{b2m+1} are turned on, the circuit forms the switched-capacitors resonant tanks as shown in Figure 5. In the state of the ZCS-SC, charge will transfer from SC_k to C_k switched-capacitor tank when the voltage of SC_k is higher than the initial voltage of C_k. Therefore, C_k is charged and the control signal during the process is shown in the top curve of Figure 5 and Table 1. In a similar way, the charge will transfer from C_j to SC_j when the voltage of SC_j is lower than the initial voltage of C_j. C_j is discharged in this process and the control signal is shown in the bottom curve of Figure 5 and Table 1. SC_k, C_k, L_k and SC_j, C_j, L_j form the resonant loops. The r_{SC}, r_C, r_S, and r_L internal resistors for SCs, switched-capacitors, ON-resistance of the switches, and inductors, respectively. In order to simplify the operation analysis, the internal resistance will first be ignored. All the components are ideal.

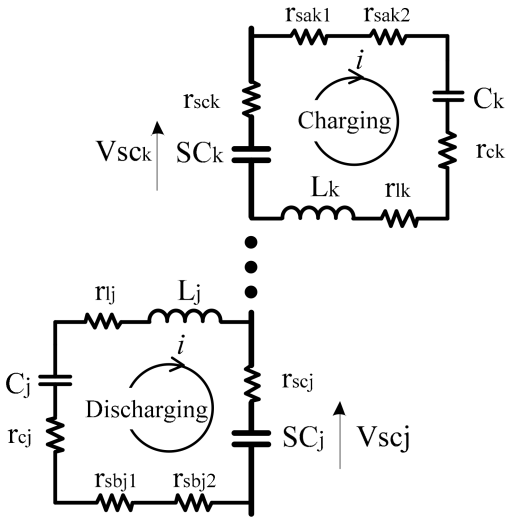

Figure 5. Circuit of ZCS mode.

Table 1. Switches control logical signal.

Function Mode	Switching States							
	S_{a2m-1}	S_{a2m}	S_{a2m+1}	S_{a2m+2}	S_{b2m-1}	S_{b2m}	S_{b2m+1}	S_{b2m+2}
ZCS mode	1	0	1	0	1	0	1	0
Buck boost mode	1	1	0	0	1	1	0	0

(1) State I (See Figure 5 charging circle)

In the state when S_{a2m-1} and S_{a2m+1} are turned on and S_{a2m} and S_{a2m+2} are turned off. Assume that all the components here are ideal and there is zero internal resistance for the SCs, switched-capacitors, inductors, and switches in this analysis. The relationship between the current and the voltage are as shown below:

$$i_r = C_k \frac{dV_{C_k}}{dt} \tag{2}$$

$$L_k \frac{di_r}{dt} + V_{C_k} = V_{SC_k} \tag{3}$$

where L_k is the inductance of inductor L_k; V_{SCk} is the voltage of SC_k.

Then, the variations of the V_{Ck} and i_r of the above are

$$V_{C_k} = V_{SC_k} - \frac{\Delta V_{C_k}}{2} \cos(\omega t) \tag{4}$$

$$i_r = I_r \sin(\omega t) \tag{5}$$

where ΔV_{Ck} is the peak-to-peak amplitude of V_{Ck}; I_r is the amplitude of the i_r; ω is the resonant angular frequency which is $\omega = \frac{1}{\sqrt{L_k C_k}}$, C_k is the capacitance of C_k.

In this resonant period, assume that the initial voltage $V_{C\min}$ across the capacitor C_k is minimum voltage, which is lower than the voltage V_{SCk} across the SC_k. The initial voltage V_{Lk} and the amplitude of the i_r are:

$$V_{Lk} = L_k \frac{di_r}{dt} = V_{SC_k} - V_{C_{\min}} \tag{6}$$

$$I_r = \frac{V_{SC_k} - V_{C_{\min}}}{\omega L_k} = \left(V_{SC_k} - V_{C_{\min}}\right) \sqrt{\frac{C_k}{L_k}} \tag{7}$$

After half a resonant period, the voltage of the V_{Ck} could reach maximum $V_{Ck\_\max}$, which is shown below:

$$V_{C_k\_\max} = 2V_{SC_k} - V_{C_{\min}} \tag{8}$$

(2) State II (See Figure 5 discharging circle)

In the state when S_{b2m-1} and S_{b2m+1} are turned on and S_{b2m} and S_{b2m+2} are turned off, the switched-capacitor C_j is discharging SC_j and the resonant current i_r is increasing in the opposite direction. Similarly as state I, the amplitude of the resonant current is

$$I_r = \frac{V_{C_{\max}} - V_{SC_j}}{\omega L_j} = \left(V_{C_{\max}} - V_{SC_j}\right) \sqrt{\frac{C_j}{L_j}} \tag{9}$$

The voltage of V_{Cj} could reach minimum $V_{Cj\_\min}$ at the end of this resonant period.

$$V_{C_j\_\min} = 2V_{SC_j} - V_{C_{\max}} \tag{10}$$

In fact, there are equivalent series resistance (ESR) for the components and the voltage drop across the switches that cannot be ignored. The r_{SC}, r_C, r_S, and r_L internal resistors for SCs, switched-capacitors,

ON-resistance of the switches and inductors respectively should be considered in the following analysis. The total ESR R_{ESR} in one resonant tank of the circuit is $R_{ESR} = r_{SC} + r_C + r_L + 2r_S$.

The resonant current of charging and discharging state should be revised as:

State I:

$$i_r = \frac{V_{SC_k} - V_{C_{\min}}}{\omega_r L_k} e^{-\rho t} \sin \omega_r t \tag{11}$$

State II:

$$i_r = \frac{V_{C_{\max}} - V_{SC_j}}{\omega_r L_j} e^{-\rho t} \sin \omega_r t \tag{12}$$

where $\rho = \frac{R_{ESR}}{2L_{k,j}}$, $\omega_r = \sqrt{\frac{1}{L_{k,j}C_{k.j}} - \rho^2}$.

$L_{k,j}$ refers to either L_k or L_j in each of their state I and II and hence ρ and ω_r are calculated according to their respective L_k or L_j in State I and State II. The maximum and minimum voltage of $V_{Ck,j}$ are

$$V_{C_{\max}} = V_{SC_k} + \left(V_{SC_k} - V_{C_{\min}}\right) e^{-\rho\pi/\omega_r} \tag{13}$$

$$V_{C_{\min}} = V_{SC_j} - \left(V_{C_{\max}} - V_{SC_j}\right) e^{-\rho\pi/\omega_r} \tag{14}$$

3. Modeling for Balancing Mode

3.1. Modeling for ZCS Balancing Mode

As it is shown in Figure 6, SC cells can be formulated to be charged or discharged between each other with the equivalent resistance. In the resonant circuit, C_k, L_k and C_j, L_j has the same value C and L, respectively, and all the switches are the same. The voltage of V_C could achieve the maximum V_{C_max} at the end of the state I and be reduced to the minimum at the end of state II. The voltage ripple ΔV_C can be obtained by subtracting (14) from (13).

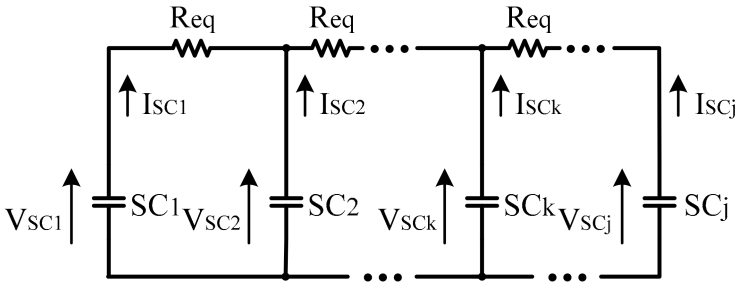

Figure 6. Model of the ZCS mode circuit.

$$\Delta V_C = \left(V_{SC_k} - V_{SC_j}\right) \frac{1 + e^{-\rho\pi/\omega_r}}{1 - e^{-\rho\pi/\omega_r}} \tag{15}$$

In one switching cycle the quantity of electric charge is $C\Delta V_C$, flowing from higher voltage cell to lower voltage cell. The average current I_{avg_r} of one cycle is

$$I_{avg\_r} = f_s \cdot C \cdot \Delta V_C \tag{16}$$

When ΔV_C in (15) is substituted into (16), the equivalent resistance R_{eq} of each resonant tank is

$$R_{eq} = \frac{1 - e^{-\rho\pi/\omega_r}}{f_s C\left(1 + e^{-\rho\pi/\omega_r}\right)} \tag{17}$$

The power loss P_{loss_r} of the ZCS mode is shown below

$$P_{loss\_r} = I_{avg\_r}^2 \cdot R_{eq} = f_s C\left(V_{SC_k} - V_{SC_j}\right)^2 \frac{1 + e^{-\rho\pi/\omega_r}}{1 - e^{-\rho\pi/\omega_r}} \tag{18}$$

3.2. Modeling for Buck-Boost Balancing Mode

During the progress of the buck-boost balancing mode, the charging/discharging varies in one cycle, the charge is transferred between SC_k and SC_j. The equivalent model of the balancing circuit is shown in Figure 7, where the ESR and the on-state voltage for the diode are included to facilitate modeling.

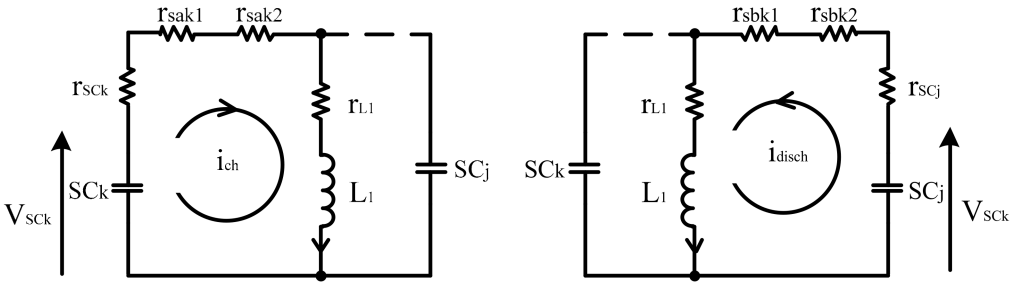

Figure 7. Model of the buck-boost mode circuit under charging and discharge.

To illustrate the voltage conversion process for the inductor L_1, the mmf values of $M_{\_ch}$ and $M_{\_disch}$ to investigate the voltage conversion of the converter circuit for charging and discharging, respectively, during one cycle are

$$M_{\_ch} = \frac{V_{SCk}}{L_1} D_1 T \tag{19}$$

$$M_{\_disch} = \frac{V_{SCj}}{L_1} D_2 T \tag{20}$$

where D_1 and D_2 are the turn-on duty ratio of switches for charging and discharging, respectively, $D_1 + D_2 = 1$.

Considering volt-second balancing of L_1, the relationship between two cells is

$$V_{SCk} DT - R_1 \int_{t_1}^{t_2} i_{ch} dt = V_{SCj}(1 - D)T - R_2 \int_{t_2}^{t_3} i_{disch} dt \tag{21}$$

where $R_1 = 2r_S + r_L + r_{SCk}$, $R_2 = 2r_S + r_L + r_{SCj}$; i_{ch} and i_{disch} are instantaneous current across L_1 for charging and discharging, respectively. I_{avg_ch} and I_{avg_disch} are the average current across L_1 when it is charging or discharging.

When $\int_{t_1}^{t_2} i_{ch} dt \approx I_{avg\_ch} DT$ and $\int_{t_2}^{t_3} i_{disch} dt \approx I_{avg\_disch}(1 - D)T$, I_{avg_ch} could be obtained from (21) as:

$$I_{avg\_ch} = \frac{V_{SCj}(1 - D) + V_{SCk} D}{R_2(1 - D) + R_1 D} \tag{22}$$

The average current I_{avg_b} of SC in this mode is

$$I_{avg\_b} = \frac{V_{SCj}(1 - D)D + V_{SCk} D^2}{R_2(1 - D) + R_1 D} \tag{23}$$

In the balancing progress, all the energy transfers between each cell, from the higher voltage SC cell to lower voltage cell. During these states, the variation of the i_{ch} is

$$i_{ch}(t) = I_{avg\_ch} + \Delta i_{ch}\left(t - \frac{DT}{2}\right) \tag{24}$$

where Δi_{ch} is the current difference during charging state, $T = \frac{1}{f_s}$.

The variation of the i_{disch} is

$$i_{disch}(t) = I_{avg\_disch} + \Delta i_{disch}\left(t - \frac{DT}{2}\right) \tag{25}$$

where Δi_{disch} is the current difference during discharging state.

The energy discharged E_{disch} from SC_k and the energy charged E_{ch} to the SC_j throughout one cycle are:

$$E_{disch} \approx V_{SCk}\int_{t_1}^{t_2} i_{ch}dt \tag{26}$$

$$E_{ch} \approx V_{SCj}\int_{t_2}^{t_3} i_{disch}dt \tag{27}$$

The energy transferred in the inductor L_1 is

$$\int_{t_1}^{t_2}(V_{SCk} - i_{ch}R_1)i_{ch}dt \approx \int_{t_2}^{t_3}\left(V_{SCj} - i_{disch}R_2\right)i_{disch}dt \tag{28}$$

The energy loss E_{loss} could be obtained by subtracting Equation (27) from (26).

$$\begin{aligned} E_{loss} &\approx V_{SCk}\textstyle\int_{t_1}^{t_2} i_{ch}dt - V_{SCj}\int_{t_2}^{t_3} i_{disch}dt \\ &= R_1\textstyle\int_0^{DT} i_{ch}^2 dt + R_2\int_0^{(1-D)T} i_{disch}^2 dt \\ &= T\left(I_{avg\_ch}^2 + \frac{3\Delta i_{ch}^2}{4}\right)[R_1 D + R_2[1-D]] \end{aligned} \tag{29}$$

where $\Delta i_{ch} \approx \frac{DV_{SCk}}{2L_1 f_s}$.

The power loss P_{loss_b} of the buck-boost mode is

$$P_{loss\_b} = \frac{\left[V_{SCk}[1-D] + V_{SCj}D\right]^2}{R_2(1-D) + R_1 D} + \frac{3}{4}\left(\frac{DV_{SCk}}{L_1 f_s}\right)^2[R_2[1-D] + R_1 D] \tag{30}$$

4. Simulation Results of the Multi-Function Voltage Equalizer

In PSIM software, the proposed circuit is simulated. The circuit topologies of three series connected SCs with initial voltages of 2.0, 2.4, 2.6 V, respectively, and with the same capacitance 1F are built in the simulation shown in Figure 8. Switched-capacitors C = 22 μF are used in simulation while f_s = 15, 20, 25 kHz and 90, 100, 110 kHz of the control signals are used to operate the circuit. The above configurations are the same with practical application, except the capacitance of the SCs.

Table 2 illustrates the comparison of the waveforms in the simulation varied with a different switching frequency f_s for ZCS and buck-boost mode. It is observed that V_{SC1}, V_{SC2}, and V_{SC3} finally converge to the same voltage level in all circumstances. For the ZCS mode, when f_s is larger, the switching speed is faster that accelerates the equalization process.

Figure 9 shows the simulation results of the ZCS mode under 20 kHz frequency with 350 F SCs. At 32 s the balancing progress was about 10%, the voltage between V_{SC1} and V_{SC2} are 0.18 V at this moment. The balancing progress reached approximately 90% at 290 s when the difference reduces to 0.02 V. And the variations of the voltage of the switched-capacitor C_1 and current I_1 are shown in this figure.

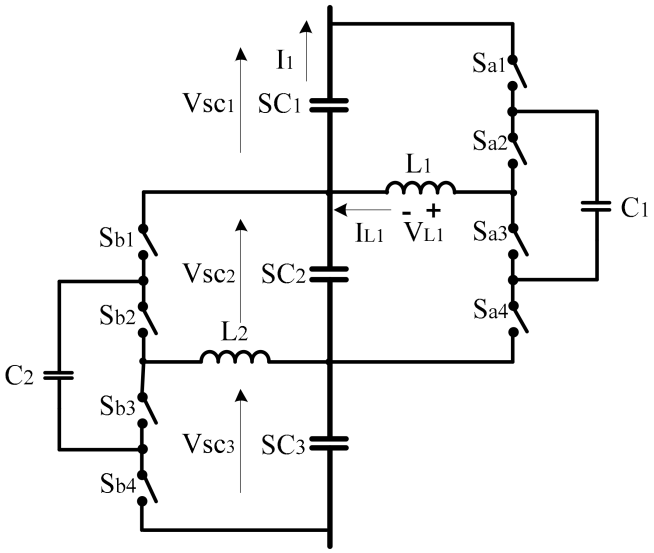

Figure 8. Multi-functional equalizer built in laboratory.

Table 2. Simulation results of the switched-capacitor voltage equalizer.

Mode	f_s = 15 kHz	f_s = 20 kHz	f_s = 25 kHz
ZCS mode	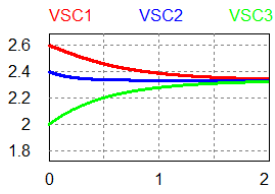	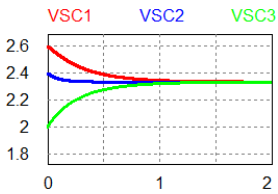	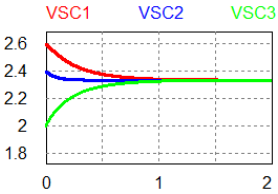
	X: Time (s); Y: Voltage (V)		
	f_s = 15 kHz	f_s = 20 kHz	f_s = 25 kHz
	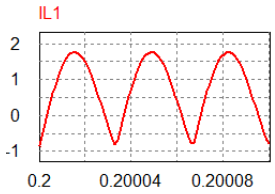	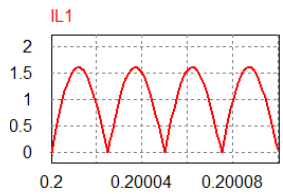	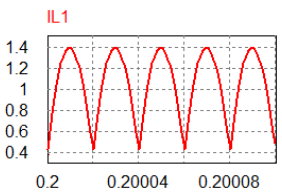
	X: Time (s); Y: Current (A)		
	f_s = 90 kHz	f_s = 100 kHz	f_s = 110 kHz
Buck-boost mode	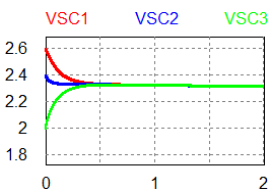	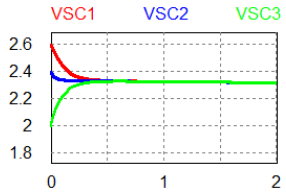	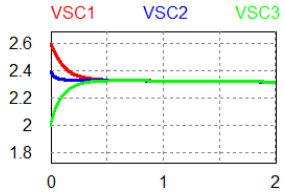
	X: Time (s); Y: Voltage (V)		

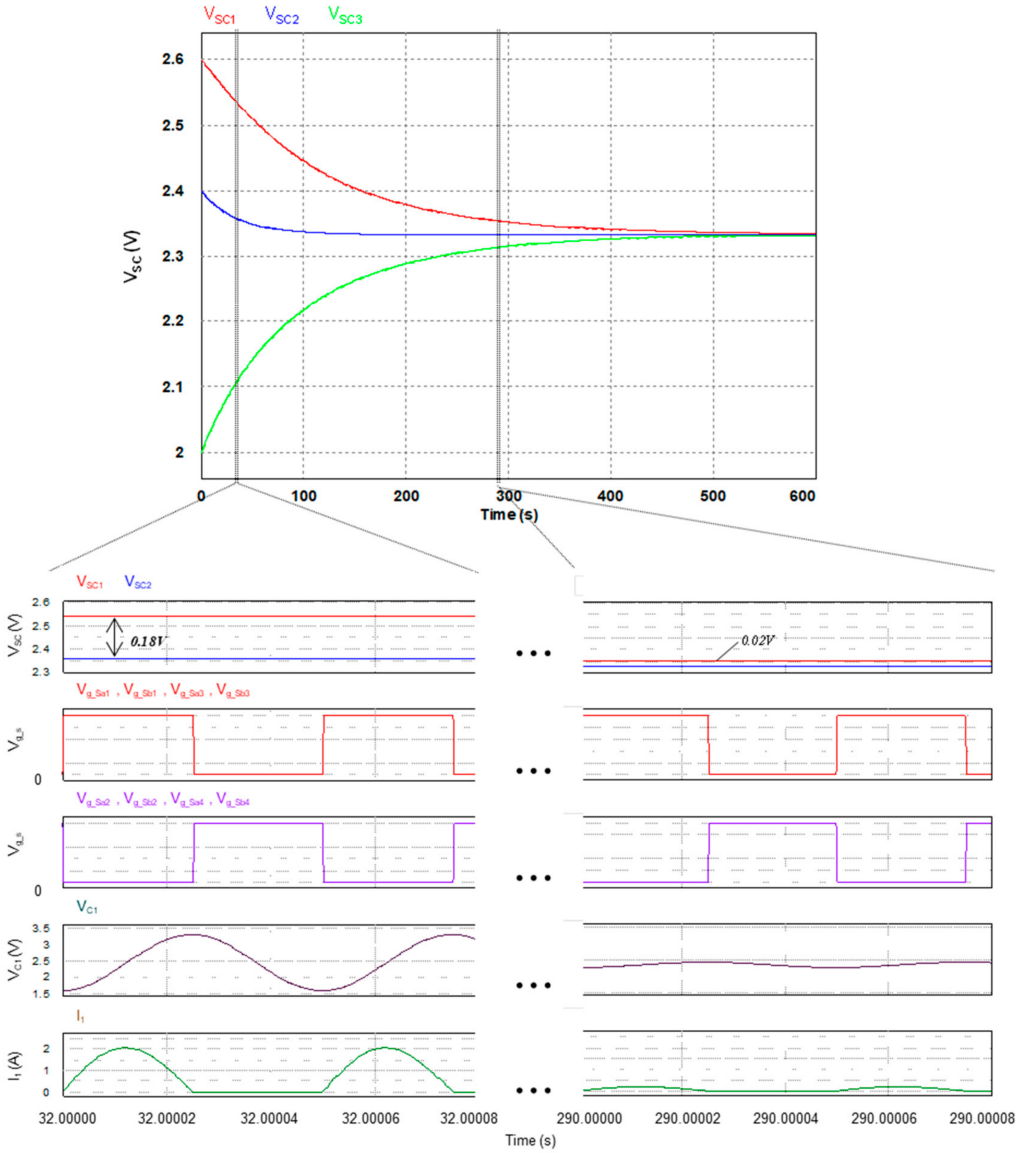

Figure 9. Simulation results of ZCS mode under 20 kHz frequency with 350 F SCs.

The balancing phenomenon conforms to the principles in Equation (16). When the switching frequency f_s is the same as the resonant frequency f_r the balancing progress could reach zero current when switches are turn on and off, this conforms to the principle in Equation (1). But the variation of the f_s could not affect the balancing speed for buck-boost mode which is illustrated in Equation (23).

5. Experimental Results of the Multi-Function Circuit

The proposed circuit has advantages in performing balancing for different EV driving modes so that it is more flexible for an energy storage system which has different working conditions. To verify the mathematical derivation and software simulation, energy storage strings composed of three SCs were formulated with the multi-functional balancing circuit controlled by different switching signals. The topology is shown in Figure 8 and the list of components is recorded in Table 3. Figure 10 is the supercapacitor test platform used in the laboratory.

The voltage balancing process for the ZCS mode of the experiment is shown in Figure 11. The initial voltages of the SCs are 2.6 V, 2.31 V, and 1.88 V, respectively. After the voltage balancing was conducted, V_{SC1} V_{SC2} and V_{SC3} were all finally balanced to the same voltage magnitude, which coincides with the

results in the above theoretical analysis. The integrated voltage magnitude after balancing was 2.23 V. Figure 12 depicts the voltage and current variations of C_1, C_2, and L_1. It is clearly shown that when the switch turns on/off, the instantaneous current of the resonant loop is close to zero, which conforms to the principles of ZCS and loss reduction.

The voltage balancing process for the buck-boost mode of the experiment is shown in Figure 13. The initial voltages of the SCs were set as 2.42 V, 2.29 V and 2.03 V, respectively. After conducting voltage balancing, V_{SC1} V_{SC2} and V_{SC3} were also balanced to the same voltage magnitude, as expected. The integrated voltage magnitude after balancing operation was 2.17 V. Figure 14 depicts the voltage and current variations of L_1. The energy loss of ZCS mode decreased 35% compared with that in buck-boost mode.

Figure 10. The supercapacitor test platform.

Table 3. Parameters in the experiment.

Units	Quantity
Supercapacitor (DRL357S0TQ60SC)	3
Capacitance of SCs	350 F
MOSFET(IRFR3607PBF) 75 V 7.34 mΩ	8
ON-resistance of MOSFETs	7.34 mΩ
Switched-capacitor (RNS1E220MDN1KX)	2
Capacitance of Switched-capacitors	22 μF
ESR of Switched-capacitors	28 mΩ
Inductor (WE-HCF)	2
Inductance of the inductor	3.3 μH
ESR of Inductor	1.31 mΩ
Switching frequency	20 kHz, 100 kHz

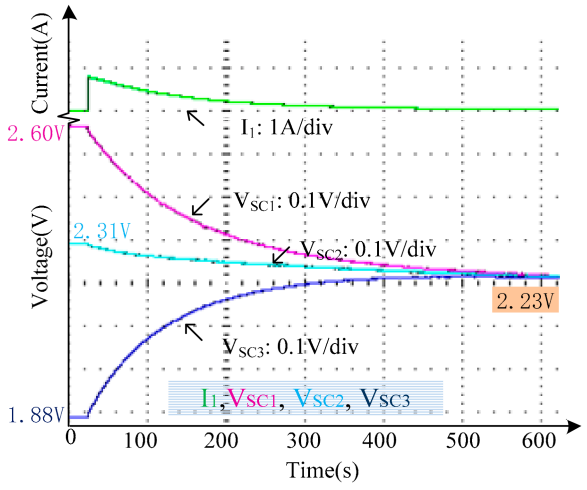

Figure 11. The ZCS mode balancing waveform from the experiment in the laboratory.

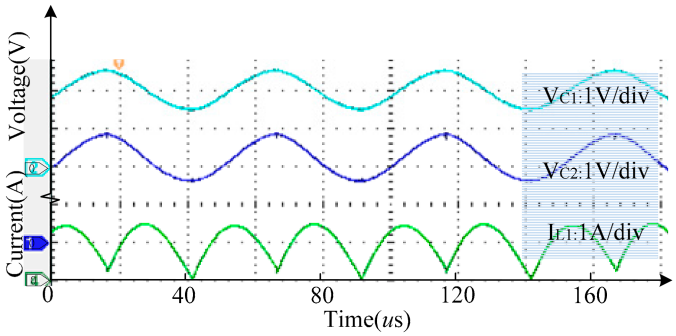

Figure 12. The voltage $V_{C1,2}$ and current I_{L1} waveform of switched-capacitor C_1 during the balancing progress of ZCS mode.

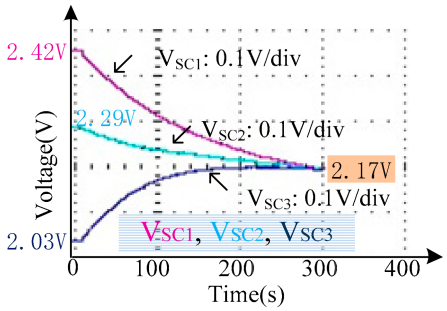

Figure 13. The buck-boost mode balancing waveform from the experiment in the laboratory.

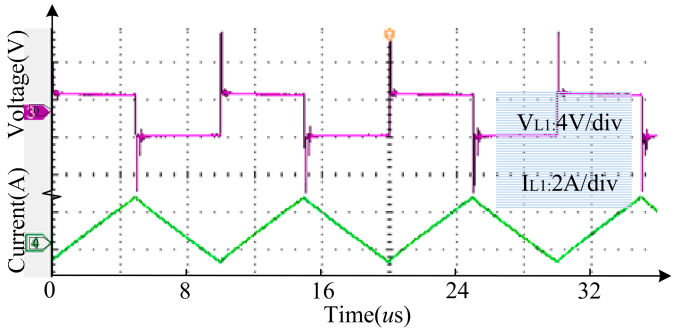

Figure 14. The voltage V_{L1} and current I_{L1} waveform of switched-capacitor C_1 during the balancing progress of buck-boost mode.

The experimental results demonstrate that the variations of both voltage and current in the proposed circuit conform to the charging/discharging principles analyzed in each phase.

6. Conclusions

A novel zero-current switching cell balancing circuit is proposed in this paper to decrease switching loss during balancing process. Furthermore, in order to adjust to different requirements of EV operation states, the multi-functional circuit was able to easily change between buck-boost and switched-capacitor pattern with flexible switching frequency and duty ratios. Simulation and field experiment were conducted to demonstrate its loss reduction effect and flexibility in various situations. The energy loss of the ZCS mode decreased 35% compared with that in the buck-boost mode. Future works may include voltage feedback control during the balancing process to further increase speed and decrease loss.

Author Contributions: X.W. proposed the theoretical models and conducted the experiment, K.W.E.C. gave the supervision and the ideas of the research work and Y.C.F. provided guidance and key suggestions.

Funding: This research was funded by Research Office, The Hong Kong Polytechnic University, Grant number G-YBLH.

Acknowledgments: The author gratefully thanks the support of Green Power Research Study 845G of The Hong Kong Polytechnic University.

Conflicts of Interest: The authors declare no conflict of interest.

References

1. Fotouhi, A.; Auger, D.J.; Propp, K.; Longo, S. Electric vehicle battery parameter identification and SOC observability analysis: NiMH and Li-S case studies. *IET Power Electron.* **2017**, *10*, 1289–1297. [CrossRef]
2. Kandasamy, K.; Vilathgamuwa, D.M.; Madawala, U.K.; Tseng, K.-J. Inductively coupled modular battery system for electric vehicles. *IET Power Electron.* **2016**, *9*, 600–609. [CrossRef]
3. Ju, F.; Deng, W.; Li, J. Performance Evaluation of Modularized Global Equalization System for Lithium-Ion Battery Packs. *IEEE Trans. Automat. Sci. Eng.* **2016**, *13*, 986–996. [CrossRef]
4. Brando, G.; Dannier, A.; Spina, I.; Tricoli, P. Integrated BMS-MMC Balancing Technique Highlighted by a Novel Space-Vector Based Approach for BEVs Application. *Energies* **2017**, *10*, 1628. [CrossRef]
5. Guo, X.; Kang, L.; Huang, Z.; Yao, Y.; Yang, H. Research on a Novel Power Inductor-Based Bidirectional Lossless Equalization Circuit for Series-Connected Battery Packs. *Energies* **2015**, *8*, 5555–5576. [CrossRef]
6. Ye, Y.; Cheng, K.W.E. An Automatic Switched-Capacitor Cell Balancing Circuit for Series-Connected Battery Strings. *Energies* **2016**, *9*, 138. [CrossRef]
7. Xu, A.; Xie, S.; Liu, X. Dynamic voltage equalization for series connected ultracapacitors in EV/HEV applications. *IEEE Trans. Veh. Technol.* **2009**, *58*, 3981–3987.
8. Choudhury, A.; Pillay, P.; Williamson, S.S. Comparative Analysis Between Two-Level and Three-Level DC/AC Electric Vehicle Traction Inverters Using a Novel DC-Link Voltage Balancing Algorithm. *IEEE J. Emerg. Sel. Top. Power Electron.* **2014**, *2*, 529–540. [CrossRef]
9. Shili, S.; Hijazi, A.; Sari, A.; Lin-Shi, X.; Venet, P. Balancing circuit new control for supercapacitor storage system lifetime maximization. *IEEE Trans. Power Electron.* **2017**, *32*, 4939–4948. [CrossRef]
10. Chemali, E.; Preindl, M.; Malysz, P.; Emadi, A. Electrochemical and Electrostatic Energy Storage and Management Systems for Electric Drive Vehicles: State-of-the-Art Review and Future Trends. *IEEE J. Emerg. Sel. Top. Power Electron.* **2016**, *4*, 1117–1134. [CrossRef]
11. Cheng, K.W.E.; Divakar, B.P.; Wu, H.; Ding, K.; Ho, H.F. Battery-Management System (BMS) and SOC Development for Electrical Vehicles. *IEEE Trans. Veh. Technol.* **2011**, *60*, 76–88. [CrossRef]
12. Cao, J.; Schofield, N.; Emadi, A. Battery balancing methods: A comprehensive review. In Proceedings of the IEEE Vehicle Power and Propulsion Conference, Harbin, China, 3–5 September 2008; pp. 1–6.
13. Shang, Y.; Zhang, C.; Cui, N.; Guerrero, J.M. A Cell-to-Cell Battery Equalizer with Zero-Current Switching and Zero-Voltage Gap Based on Quasi-Resonant LC Converter and Boost Converter. *IEEE Trans. Power Electron.* **2015**, *30*, 3731–3747. [CrossRef]
14. Lee, Y.-S.; Cheng, M.-W. Intelligent Control Battery Equalization for Series Connected Lithium-Ion Battery Strings. *IEEE Trans. Ind. Electron.* **2015**, *52*, 1297–1307. [CrossRef]
15. Ye, Y.; Cheng, K.W.E.; Liu, J.; Ding, K. A Step-Up Switched-Capacitor Multilevel Inverter with Self-Voltage Balancing. *IEEE Trans. Ind. Electron.* **2014**, *61*, 6672–6680. [CrossRef]
16. Ragheb, A.N.; Kim, H.W. Reference-Free Dynamic Voltage Scaler Based on Swapping Switched-Capacitors. *Energies* **2019**, *12*, 625. [CrossRef]
17. Khodaparast, A.; Azimi, E.; Azimi, A.; Adabi, M.E.; Adabi, J.; Pouresmaeil, E. A New Modular Multilevel Inverter Based on Step-Up Switched-Capacitor Modules. *Energies* **2019**, *12*, 524. [CrossRef]
18. Rodič, M.; Milanovič, M.; Truntič, M.; Ošlaj, B. Switched-Capacitor Boost Converter for Low Power Energy Harvesting Applications. *Energies* **2018**, *11*, 3156. [CrossRef]
19. Wang, X.; Eric Cheng, K.W.; Fong, Y.C. Non-equal voltage cell balancing for Battery and super-capacitor management system using coupled inductor techniques. *Energies* **2018**, *11*, 1037. [CrossRef]
20. Wang, X.; Eric Cheng, K.W.; Fong, Y.C. Series-Parallel Switched-Capacitor Balancing Circuit for Hybrid Source Package. *IEEE Access* **2018**, *6*, 34254–34261. [CrossRef]
21. Pascual, C.; Krein, P.T. Switched capacitor system for automatic series battery equalization. In Proceedings of the APEC 97—Applied Power Electronics Conference, Atlanta, GA, USA, 27 February 1997; pp. 848–854.

22. Baughman, A.C.; Ferdowsi, M. Double-tiered switched-capacitor battery charge equalization technique. *IEEE Trans. Ind. Electron.* **2008**, *55*, 2277–2285. [CrossRef]
23. Kim, M.-Y.; Kim, C.-H.; Kim, J.-H.; Moon, G.-W. A chain structure of switched capacitor for improve cell balancing speed of lithium-ion batteries. *IEEE Trans. Ind. Electron.* **2014**, *61*, 3989–3999. [CrossRef]
24. Cheng, K.W.E.; Evans, P.D. Parallel-mode extended-period quasiresonant convertor. *IEE Proc. B* **1991**, *138*, 243–251. [CrossRef]
25. Hui, S.Y.R.; Cheng, K.W.E.; Prakash, S.R.N. A fully soft-switched extended-period quasi-resonant power-factor-correction circuit. *IEEE Trans. Power Electron.* **1997**, *12*, 922–930. [CrossRef]
26. Jabbar, M.; Tehrani, U.D. Double-boost switched-resonator converter. *IET Power Electron.* **2018**, *11*, 1382–1388. [CrossRef]
27. Lin, J.Y.; Lin, Y.F.; Lee, S.Y. A Novel Multi-Element Resonant Converter with Self-Driven Synchronous Rectification. *Energies* **2019**, *12*, 715. [CrossRef]
28. Fong, Y.C.; Cheng, K.W.E.; Raman, S.R.; Wang, X. Multi-Port Zero-Current Switching Switched-Capacitor Converters for Battery Management Applications. *Energies* **2018**, *11*, 1934. [CrossRef]
29. Wang, C.S.; Li, W.; Meng, Z.; Wang, Y.F.; Zhou, J.G. Three-Phase High-Power and Zero-Current-Switching OBC for Plug-In Electric Vehicles. *Energies* **2015**, *8*, 6672–6704. [CrossRef]
30. Kutkut, N.H.; Wiegman, H.L.N.; Divan, D.M.; Novotny, D.W. Design considerations for charge equalization of an electric vehicle battery system. *IEEE Trans. Ind. Electron.* **1999**, *35*, 28–35. [CrossRef]
31. Ohno, T.; Suzuki, T.; Koizumi, H. Modularized LC resonant switched capacitor cell voltage equalizer. In Proceedings of the IECON 2014—40th Annual Conference of the IEEE Industrial Electronics Society, Dallas, TX, USA, 29 October–1 November 2014; pp. 3156–3162.
32. Lambert, S.M.; Pickert, V.; Atkinson, D.J.; Zhan, H. Transformer-Based Equalization Circuit Applied to n-Number of High Capacitance Cells. *IEEE Trans. Power Electron.* **2016**, *31*, 1334–1343. [CrossRef]
33. Chen, Y.; Liu, X.; Cui, Y.; Zou, J.; Yang, S. A Multi-Winding Transformer Cell-to-Cell Active Equalization Method for Lithium-Ion Batteries With Reduced Number of Driving Circuits. *IEEE Trans. Power Electron.* **2016**, *31*, 4916–4929. [CrossRef]
34. Ye, Y.M.; Eric Cheng, K.W. Quadratic boost converter with low buffer capacitor stress. *IET Power Electron.* **2014**, *7*, 1162–1170. [CrossRef]
35. Ye, Y.M.; Cheng, K.W.E.; Liu, J.F.; Xu, C. A Family of Dual-Phase-Combined Zero-Current Switching Switched-Capacitor Converters. *IEEE Trans Power Electron.* **2014**, *29*, 4209–4218. [CrossRef]
36. Zhang, Y.; Zhang, Y.; Ai, Z.; Feng, Y.; Cheng, W.; Hu, Z. Energy Saving Control Strategy for the High-Frequency Start-up Process for Electric Mining Haul Trucks. *IEEE Trans. Intell. Veh.* **2018**, *3*, 595–606. [CrossRef]
37. Zhang, S.; Luo, Y.; Wang, J.; Wang, X.; Li, K. Predictive Energy Management Strategy for Fully Electric Vehicles Based on Preceding Vehicle Movement. *IEEE Trans. Intell. Transp. Syst.* **2017**, *18*, 3049–3060. [CrossRef]
38. Rezaei, A.; Burl, J.B.; Rezaei, M.; Zhou, B. Catch Energy Saving Opportunity in Charge-Depletion Mode, a Real-Time Controller for Plug-In Hybrid Electric Vehicles. *IEEE Trans. Veh. Technol.* **2018**, *67*, 11234–11237. [CrossRef]
39. Yuan, J.S.; Bi, Y. Process and temperature robust voltage multiplier design for RF energy harvesting. *Microelectron. Reliab.* **2014**, *55*, 107–113. [CrossRef]
40. Yuan, J.S.; Xu, Y.; Yen, S.D.; Bi, Y.; Hwang, G.W. Hot carrier injection stress effect on a 65 nm lna at 70 ghz. *IEEE Trans. Device Mater. Reliab.* **2014**, *14*, 931–934. [CrossRef]

© 2019 by the authors. Licensee MDPI, Basel, Switzerland. This article is an open access article distributed under the terms and conditions of the Creative Commons Attribution (CC BY) license (http://creativecommons.org/licenses/by/4.0/).